

Sources of Third–Order Intermodulation Distortion in Bulk Acoustic Wave Devices: A Phenomenological Approach

Eduard Rocas and Carlos Collado
*Universitat Politècnica de Catalunya (UPC), Barcelona
Spain*

1. Introduction

Acoustic devices like Bulk Acoustic Wave (BAW) resonators and filters represent a key technology in modern microwave industry. More specifically, BAW technology offers promising performance due to its good power handling and high quality factors that make it suitable for a wide range of applications. Nevertheless, harmonics and 3IMD arising from intrinsic nonlinear material properties (Collado et al., 2009) and dynamic self-heating (Rocas et al., 2009) could represent a limitation for some applications.

Driven by the need for highly linear devices, there is a demand for further development of accurate models of BAW devices, capable of predicting the nonlinear behavior of the device and its impact on a circuit. Many authors have attempted to model the nonlinearities of BAW devices by using different approaches, mostly involving phenomenological lumped element models. Although these models can be useful because of their simplicity, they are mainly limited to narrow-band operation and they usually cannot be parameterized in terms of device-independent parameters (Constantinescu et al., 2008). Another approach consists of extending all the material properties on the constitutive equations to the nonlinear domain and introducing the nonlinear relations to the model implementation, which leads to several possible nonlinear sources increasing model complexity (Cho et al., 1993; Ueda et al., 2008). On the other hand, (Feld, 2009) presents a one-parameter nonlinear circuit model to account for the intrinsic nonlinearities. Such a model does not include the self-heating mechanism and can underestimate the 3IMD by more than 20 dB.

In this work, a model that uses several nonlinear parameters to predict harmonics and 3IMD distortion is presented. Its novelty lies in its ability to predict the nonlinear effects produced by self-heating in addition to those due to intrinsic nonlinearities in the material properties. The model can be considered an extension of the nonlinear KLM model (originally proposed by Krimholtz, Leedom and Matthaei) (Krimholtz et al., 1970) to include the thermal effects due to self-heating caused by viscous losses and electrode losses. For this purpose a thermal domain circuit model is implemented and coupled to the electro-acoustic model, which allows us to calculate the dynamic temperature variations that change the material properties. In comparison to (Rocas et al., 2009), this work describes the impact that electrode losses produce on the 3IMD, presents closed-form expressions derived from the

circuit model and validates the model with extensive measurements that confirm the necessity to include dynamic self-heating to accurately predict the generation of spurious signals in BAW devices.

2. Nonlinear generation mechanisms

The origin of nonlinearities in BAW resonators has been controversial and there still exists no consensus (Nakamura et al., 2010). However, recent results point to several underlying causes which combine in different ways to give rise to a wide range of nonlinear effects (Rocas et al., 2009). We summarize the nonlinear effects of a stiffened elasticity, and then address the nonlinearity due to self-heating caused by viscous losses and electrode losses. We develop a circuit model to describe self-heating effects, and compare the measured results with simulations. Closed-form expressions for a simple one-layer BAW device model are then extracted to better understand the nonlinear generation mechanisms.

2.1 Nonlinear stiffened elasticity

Nonlinear elasticity has been proposed as the predominant contribution to the measured second harmonics and as a potential source of the observed 3IMD products (Collado et al., 2009) in two-tone experiments.

The approach described in (Collado et al., 2009) starts by considering a nonlinear stress-strain relation under electric field described by a nonlinear stiffened elasticity $c^D(T)$ in the form of the polynomial

$$c^D(T) = c_0^D + \Delta c_1^D T + \Delta c_2^D T^2 \quad (1)$$

where T is the stress. As detailed in (Collado et al., 2009), (1) translates into a nonlinear distributed capacitance $C_d(v)$ in the equivalent electric model of the acoustic transmission line (Auld, 1990), in which the voltage v is equivalent to force. In the equivalent electric model (1) transforms into:

$$C_d(v) = C_{d,0} + \Delta C_1 v + \Delta C_2 v^2. \quad (2)$$

Equation (2) leads to the nonlinear acoustic Telegrapher's equations which can be used to obtain the maximum voltage amplitude occurring along a resonating transmission line as shown in (Collado et al., 2009; Collado et al., 2005). When the device is driven by two tones at frequencies ω_1 and ω_2 , standing waves with maximum force amplitudes V_{ω_1} and V_{ω_2} are trapped in the line. Then, as detailed in (Collado et al., 2009), the nonlinear capacitance (2) is responsible for generating 3IMD signals that result from adding the contributions due to Δc_1^D and Δc_2^D :

$$V_{\omega_{12}} = A_1 Q_L V_{\omega_1}^2 V_{\omega_2}^* \Delta C_1^2 \quad (3)$$

$$V_{\omega_{12}} = A_2 Q_L V_{\omega_1}^2 V_{\omega_2}^* \Delta C_2 \quad (4)$$

where $\omega_{12} = 2\omega_1 - \omega_2$, Q_L is the loaded quality factor and A_1 and A_2 are constants that depend on the geometry of the device and on its materials. Identical results would be obtained for the 3IMD at $2\omega_2 - \omega_1$ (which we will denote as ω_{12}).

2.2 Self-heating

Third-order intermodulation distortion due to dynamic self-heating is a well known process in microwave power amplifiers (Camarchia et al., 2007; Parker et al., 2004; Vuolevi et al., 2001) but has received less attention in passive devices (Rocas et al., 2010). What makes it different from the 3IMD caused by intrinsic nonlinearities is its dependence on the envelope frequency of the signal. For the particular case of a two-tone experiment, in which the envelope is a sinusoid, the thermal generation of 3IMD has a low-pass dependence on the envelope frequency due to the slow dynamics related with heating effects.

Recent results of two-tone 3IMD tests in BAW resonators as a function of the tones spacing reveal the important impact of self-heating effects in thin-Film Bulk Acoustic Resonators (FBAR) (Collado et al., 2009; Feld, 2009; Rocas et al., 2008) and Solidly Mounted Resonators (SMR) (Rocas et al., 2009). Heating produced by viscous damping in the acoustic domain and by ohmic loss in the electric domain produce local temperature oscillations which affect the temperature-dependent material properties.

If $\omega_1 = \omega_0 - \Delta\omega/2$ and $\omega_2 = \omega_0 + \Delta\omega/2$ are the input signals for a two-tone test, dissipation occurs as a result of electric and acoustic losses, and the quadratic dependence of the dissipated power on the signal amplitude

$$P_d \propto \left(V_1 \cos\left(\left(\omega_0 - \frac{\Delta\omega}{2}\right)t\right) + V_2 \cos\left(\left(\omega_0 + \frac{\Delta\omega}{2}\right)t\right) \right)^2 \quad (5)$$

gives rise to several frequency components of the dissipated power:

$$\begin{aligned} P_d \propto & \frac{1}{2}V_1^2 + \frac{1}{2}V_2^2 + \frac{1}{2}V_1^2 \cos(2\omega_0 t - \Delta\omega t) + \\ & \frac{1}{2}V_2^2 \cos(2\omega_0 t + \Delta\omega t) + V_1V_2 \cos(2\omega_0 t) \\ & + V_1V_2 \cos(\Delta\omega t). \end{aligned} \quad (6)$$

These frequency components produce temperature variations on the device at the same frequencies. These temperature variations $K(\omega)$ can be written in terms of the dissipated power and the thermal impedance as (Parker et al., 2004)

$$K(\omega) = Z_{th}(\omega)P_d(\omega). \quad (7)$$

It is important to point out that the temperature variation at the envelope frequency ($\Delta\omega = \omega_2 - \omega_1$) is the most relevant for the generation of spurious signals because of the low-pass filter character of the thermal impedance $Z_{th}(\omega)$. These slow temperature oscillations induce low frequency changes of the material properties, and consequently, generate undesired 3IMD.

In addition to being able to calculate the temperature oscillations, we also need to determine how these oscillations influence the device performance. For the specific case of BAW devices, there is consensus in assuming that the detuning of BAW devices with temperature is due to the variation of multiple material properties with temperature (Lakin et al., 2000; Ivira et al., 2008; Petit et al., 2007). We reflect this in our model by adding a temperature-dependent term to the stiffened elasticity in (1)

$$c^D(T, K) = c_0^D + \Delta c_1^D T + \Delta c_2^D T^2 + \Delta c_K^D K \quad (8)$$

where K represents the temperature, the equivalent capacitance is

$$C_d(v, K) = C_{d,0} + \Delta C_1 v + \Delta C_2 v^2 + \Delta C_K K, \quad (9)$$

where each of the nonlinear terms ΔC_1 , ΔC_2 and ΔC_K are related to their counterparts ΔC_1^D , ΔC_2^D , ΔC_K^D respectively, as detailed in Appendix I.

The term ΔC_K generates 3IMD, whose maximum voltage $V_{\omega l 2}$ can be found in a similar way as the contribution of ΔC_1 in (3) and ΔC_2 in (4) (see details in Appendix I):

$$V_{\omega l 2} = A_T Q_L \Delta C_K P_{d, \Delta \omega} Z_{th, \Delta \omega}^* V_{\omega_1}, \quad (10)$$

where A_T is a constant that depends on the device geometry and material parameters, Q_L is the loaded quality factor, $Z_{th, \Delta \omega}$ is the thermal impedance (7) evaluated at $\Delta \omega$, and $P_{d, \Delta \omega}$ is the $\Delta \omega$ frequency component of the dissipated power in (6). Equation (10) describes the 3IMD signal due to self-heating effects, inside the acoustic transmission line, in terms of the dissipated power. As detailed in the following sub-sections, the dissipated power is due to both electric and acoustic loss, thus both effects contribute to the 3IMD in (10).

2.2.1 3IMD due to viscous losses

Viscosity is introduced in the model as a complex elasticity (Auld, 1990), which translates into a shunt resistance $R_{d, \eta}$ in series with the shunt capacitance C_d in a transmission line implementation. Appendix II details a model transformation to go from the original $R_{d, \eta}$ to an equivalent model in which the viscosity is implemented as a conductance G_d in parallel with the capacitance C_d . The equivalent model allows for an easier extraction of the closed-form expressions.

The instantaneous dissipated power due to viscous damping at each position z along the transmission line of length l (thickness of the piezoelectric layer) is

$$\frac{\partial P_{d, \Delta \omega}(z)}{\partial z} = G_d V_{\omega_1} V_{\omega_2} \cos^2\left(\frac{\pi z}{l}\right), \quad (11)$$

which can be integrated along l to obtain the total dissipated power

$$P_{d, \Delta \omega} = \frac{1}{2} l G_d V_{\omega_1} V_{\omega_2}^*. \quad (12)$$

Equation (12) can be combined with (10) to obtain the peak 3IMD voltage ($V_{\eta, \omega l 2}$) due to the viscous damping

$$V_{\eta, \omega l 2} = \frac{1}{2} A_T l G_d Q_L \Delta C_K Z_{th, \Delta \omega}^* V_{\omega_1}^2 V_{\omega_2}^* \quad (13)$$

2.2.2 3IMD due to loss in the electrodes

There is certain agreement in considering ohmic losses as a significant dissipation mechanism (Thalhammer et al., 2005) in addition to the viscous damping. As it will be discussed in section II.B.3, electrodes losses are introduced in the circuit model as parasitic series resistances at the input and at the output ports, and their values are determined by fitting the model to the measured scattering parameters in the linear regime. Their

contribution to the 3IMD can be calculated by the use of (10) and the power dissipated in the parasitic resistances $P_{\rho\Delta\omega}$:

$$V_{\rho,\omega_2} = A_T Q_L \Delta C_K P_{\rho\Delta\omega} Z_{th,\Delta\omega}^* V_{\omega_1} \quad (14)$$

Whereas the parasitic resistance and distributed conductance can be obtained from the measured scattering parameters, that is, they produce distinguishable measurable effect, examination of (13) and (14) looks like both self-heating mechanisms produce the same experimental observable so they may not be distinguishable. This is true if a two-tone experiment at a fixed frequency is performed, but the two effects have different frequency dependence that can be distinguished if the central frequency ω of the 2 tones is swept while keeping the tones spacing $\Delta\omega$ constant. This happens because the frequency pattern of the dissipation due to ohmic losses is different than that produced by viscous losses, as shown in Fig 1. This information is extremely useful to validate the model with 3IMD measurements by looking at the frequency dependence of the 3IMD.

Note that (13) and (14) keep the same definition of thermal impedance $Z_{th,\Delta\omega}$. This is because the electrodes and the piezoelectric layer are thin and made of good thermal conductors, so that the thermal impedance between those layers is negligible, as will be verified with the temperature simulations shown in Section III.B.2.

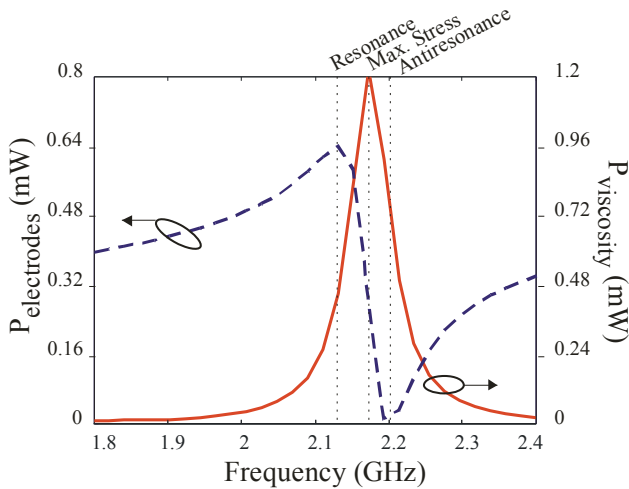


Fig. 1. Simulations of the dissipated power, for an input power of 20 dBm, due to acoustic viscous damping (solid line) and electrode electric losses (dashed line)

2.2.3 Circuit model with self-heating effects

A circuit model implementation to reproduce thermal effects should be capable of predicting dynamic temperature variations. To achieve this, we extend the nonlinear KLM model (Collado et al., 2009) to include the thermal domain (Rocas et al., 2009).

The procedure starts with the one dimensional heat equation along the z direction:

$$\frac{\partial^2 K}{\partial z^2} = \frac{\rho C_p}{k_{th}} \frac{\partial K}{\partial t} - \frac{P_d}{k_{th}}, \quad (15)$$

where the equivalent distributed parameters can be identified as the volumetric heat capacitance

$$C_{d,th} = \rho C_p \tag{16}$$

and the thermal resistance

$$R_{d,th} = \frac{1}{k_{th}} \tag{17}$$

with C_p and k_{th} being the material-specific heat capacity and thermal conductivity, respectively.

With the above-mentioned distributed parameters, a thermal distributed model can be constructed as a cascade of sections of series resistances and shunt capacitance, where each section corresponds to a specific thickness and area. Figure 2 shows a segment with $R_{th} = R_{d,th} \cdot \Delta z / A$ and $C_{th} = C_{d,th} \cdot A \cdot \Delta z$, where A is the area of the cross-section perpendicular to the z direction. In such a thermal equivalent circuit the equivalents of voltage and current are the temperature and heat respectively.

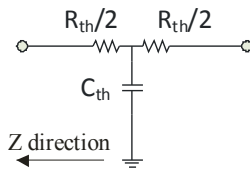


Fig. 2. Implementation of a Δz section of thermal equivalent circuit

The thermal model of a multilayer SMR can be implemented as a cascade of the previously described sections for each material, as shown in Fig. 3. The boundary conditions are the ambient temperature, modeled as a voltage source under the substrate, and the parallel combination of the radiation and convection resistances, terminated with a voltage source at ambient temperature on the upper side of the device (Larson et al., 2002).

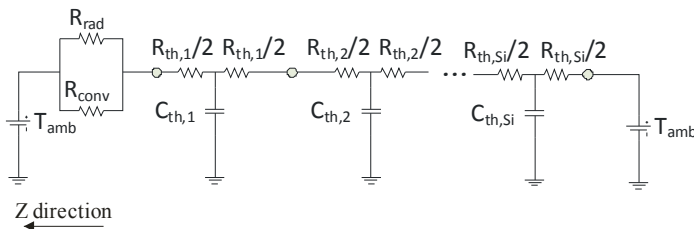


Fig. 3. Thermal model of the upper and lower materials' stacks with boundary conditions

As it can be seen from Fig. 3, the thermal impedance seen from any point along the line has a low-pass filter behavior, which means that for faster variations of the heat source, smaller temperature variations are produced.

The piezoelectric layer is implemented as a cascade of cells, in which the dissipated power due to viscous damping is directly coupled to its correspondent thermal cell. A current source is used because current is the analogue of heat in the thermal domain. The

temperature rise is used to modify the distributed acoustic capacitance $C_{NL}(T,K)$, as shown in Fig. 4.

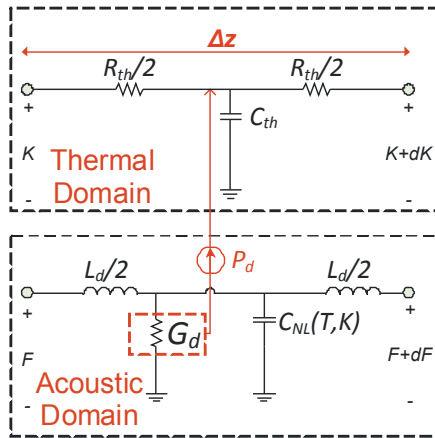


Fig. 4. Implementation of a section of the piezoelectric layer with the acoustic and thermal domains coupled by the generated heat at G_d and the temperature K . L_d is the acoustic distributed inductance $L_d = \rho \cdot A \cdot \Delta z$.

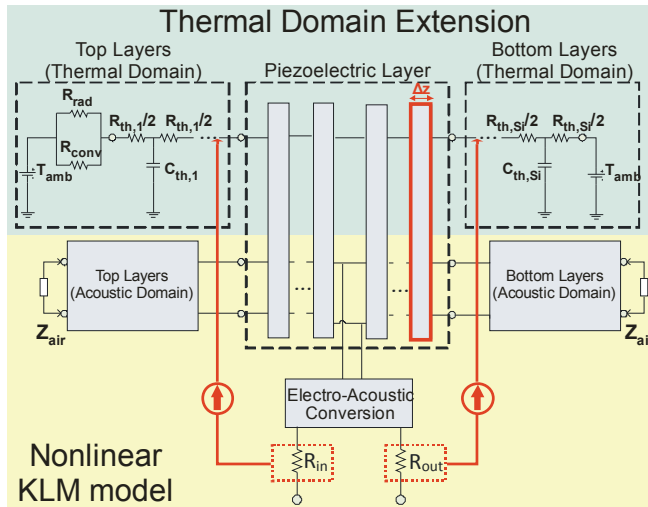


Fig. 5. Complete circuit model with thermo-acoustic model of the piezoelectric layer, top and bottom layers, and lossy electrodes. Electric losses, in the electrodes, and viscous losses, in the piezoelectric layer, produce dissipation that is coupled to the thermal domain to reproduce temperature rise. The temperature rise is used to change the material properties

On the other hand, the parasitic electrodes losses are implemented by use of a lumped resistor at the input and output of the modeled device as shown in Fig. 5. As done for the viscosity, the dissipation in each resistor is coupled to the thermal model as a heat source. In

fact, dissipation in the input and output resistors is coupled to the correspondent top and bottom thermal sections that model the electrodes. The complete model can be seen in Fig. 5, where a cell of the piezoelectric layer like that in Fig. 4, is highlighted in red.

In the figure above, the electric-acoustic conversion box includes those elements of the KLM model whose purpose is the electro-acoustic signal conversion (Krimholtz et al., 1970). Additionally, the material layers above and below the piezoelectric are shown as simplified blocks for clarity.

2.2.4 Comparison of formulation and nonlinear simulations

We use the circuit model of Fig. 5, with only a piezoelectric layer, to check the accuracy of the formulation described in the previous section. The circuit model has been simulated, reproducing a two-tone experiment, with Harmonic Balance techniques by use of a commercial CAD software. A simple model is implemented making use of 100 cells to reproduce a $1.25 \mu\text{m}$ thick and $2.33 \cdot 10^{-8} \text{ m}^2$ piezoelectric layer with a quality factor of 1800. The electrodes losses and viscous losses are coupled to a low-pass thermal impedance.

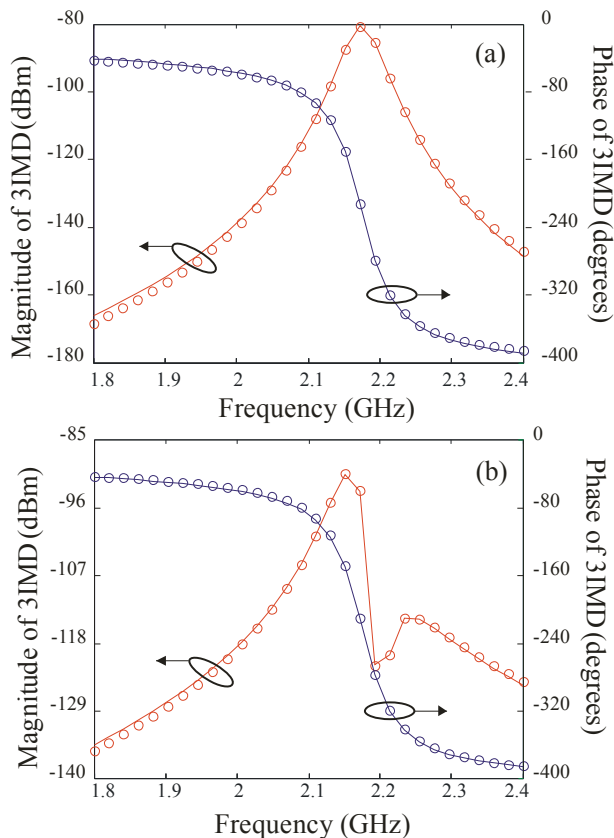


Fig. 6. Comparison of the magnitude and phase of $2\omega_1 - \omega_2$ calculated with equation (13) (circles) in Fig.6a (viscous losses, no electrode losses) and equation (14) (circles) in Fig.6b (electrode losses, no viscous losses), vs. simulation with the circuit model (solid lines)

In the first set of simulations we keep the tones spacing constant at $\Delta\omega/2\pi = 220$ Hz and sweep the central frequency ω_0 in a 600 MHz range around the resonance frequency, which is 2.18 GHz. By doing this, we can distinguish the 3IMD produced by viscous self-heating from that produced by electric self-heating by analyzing the resulting frequency dependence. In the former case, we do not connect the dissipation in the electrodes to the thermal domain (Fig.6a), whereas in the latter case we do not connect the dissipation in the piezoelectric layer to the thermal domain (Fig.6b). The 3IMD frequency dependences are a direct consequence of the frequency dependences of the dissipated power. More specifically, a minimum at the anti-resonance frequency appears in Fig. 6.b because there is minimum current flowing through the electrodes at anti-resonance, which can be used in experimental measurements to identify different sources of self-heating effects.

In the second set of simulations we keep the central frequency constant at 2.18 GHz and we change the separation between tones from 100 Hz to 1 MHz. This allows us to reproduce the low-pass filter behavior of the thermal impedance. Figure 7 shows the results of the second set of simulations for a wide range of separation between tones when the self-heating effects are due to viscous losses, where it is clear the low-pass filter behavior of the temperature induced effects. A very similar plot was obtained for electrode losses, which is not shown for simplicity.

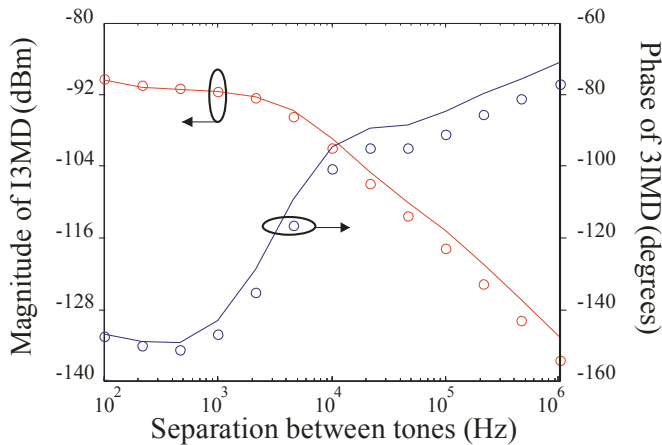


Fig. 7. Magnitude and phase of equation (13) (circles) and simulations with the circuit model (traces) for a wide range of separation between tones

Figures 6 and 7, in addition to giving useful qualitative information about the 3IMD generation due to the self-heating mechanism, show that the formulation of equations (13) and (14) is in very good agreement with the simulations, so that these expressions can be used for a better understanding of the temperature-induced 3IMD in BAW resonators.

3. Experimental results

Four state-of-the-art rectangular Solidly-Mounted Resonators (SMR) from a commercial manufacturer, with different areas summarized in Table 1, have been measured. The resonators have a $1.25 \mu\text{m}$ thick aluminum nitride layer and a W - SiO_2 Bragg mirror (alternating layers of W and SiO_2), and show quality factors around 1800.

From (8) it is clear that several sources, characterized by Δc^{D_1} , Δc^{D_2} and Δc^{D_K} , can generate 3IMD. Therefore, we follow a step-by-step procedure that includes several experiments to determine which nonlinear source is designed responsible for each observable at each experiment by use of the circuit model:

- We first adjust the linear model to the measured S-parameters of the devices, so that the electric and viscous losses can be quantified. The procedure consists of a fine tuning of the material properties.
- Second harmonic measurements are performed along the frequency range of interest to extract the intrinsic nonlinear parameter Δc^{D_1} .
- The term Δc^{D_2} also contributes to the 3IMD generation. We use the literature value in (Łepkowski et al., 2005) because this contribution cannot be independently extracted from measurements.
- Third-order intermodulation distortion measurements with sweeping the tone spacing are conducted to quantify the frequency dependence of the thermal impedance, and set the temperature coefficient of stiffened elasticity Δc^{D_K} accordingly.

3.1 Linear modeling of the devices under test

Broadband one-port S-parameters measurements of the devices have been performed after an on-wafer OSL calibration. The measurements have been done at a power level of -10 dBm to ensure the linear regime and are used to fit the linear parameters of the circuit model. The only differences between the devices are the resonator area and electrode losses.

Electric losses due to the resistivity of the electrodes are modeled as lumped parasitic resistances, so their values are dependent on the resonator area and have a broadband effect on the linear device response. Table 1 summarizes the device areas and electric resistances.

On the other hand, acoustic losses due to viscosity only have an observable effect at those frequencies where there is substantial electro-acoustic coupling, that is around resonance and anti-resonance. By using the model transformation in Appendix II, the acoustic losses that fit all devices can be described with the same material viscosity value $\eta = 0.033 \text{ N s m}^{-2}$, what verifies the validity of the linear model.

Resonator	Area (m ²)	Electric Resistance R _s (Ω)
A1	6.41e-8	0.28
A2	4.88e-8	0.37
A3	2.33e-8	0.42
A4	1.25e-8	1

Table 1. Tested devices

3.2 Nonlinear characterization

The nonlinear behavior of a BAW resonator arises from different contributions due to intrinsic nonlinear material properties and self-heating mechanisms.

3.2.1 Intrinsic nonlinearities

Intrinsic nonlinearities due to the stiffened elasticity, as shown in (1), predominate above other intrinsic nonlinear material contributions. As a consequence, the second harmonic has the same frequency dependence as the mechanical stress in the piezoelectric layer (Collado

et al., 2010). In fact, as done in (Collado et al., 2010), the second harmonic is used to extract a unique unitless value $\Delta c^D_1 = 10.5$ of the stiffened elasticity that fits the second harmonic for all the devices.

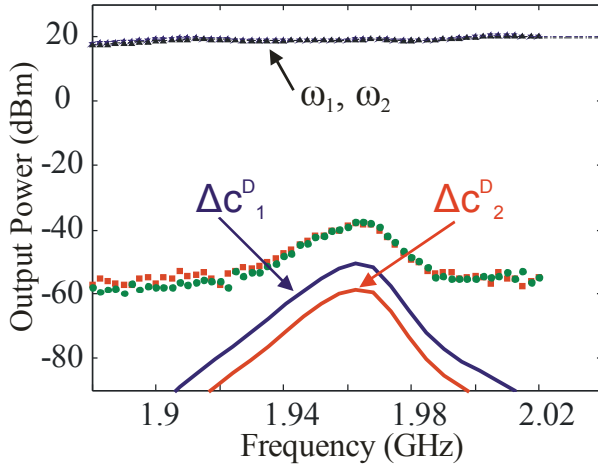


Fig. 8. 3IMD measurements (squares are $2\omega_1-\omega_2$, circles are $2\omega_2-\omega_1$) and circuit simulations of the Δc^D_1 and Δc^D_2 contributions to the 3IMD ($2\omega_1-\omega_2$ and $2\omega_2-\omega_1$ overlap). Both measurements and simulations are done for $\Delta f = 220$ Hz. The intrinsic nonlinearities are not sufficient to explain the measurements. Measurements (squares and triangles) and simulations (dashed lines) of ω_1 and ω_2 are also presented

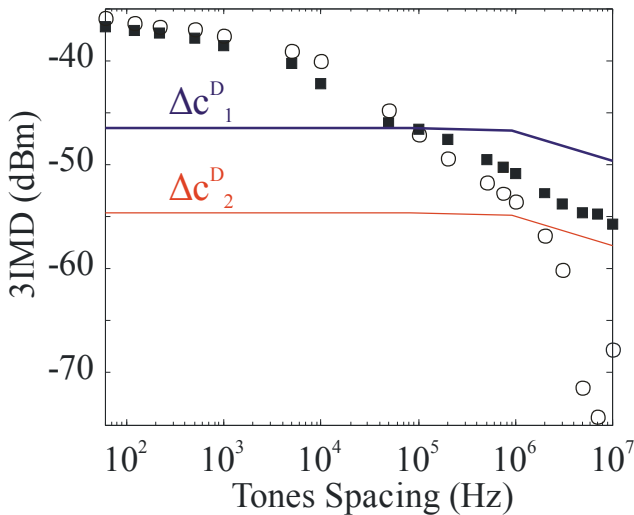


Fig. 9. 3IMD measurements (squares are $2\omega_1-\omega_2$, circles are $2\omega_2-\omega_1$) and circuit simulations of the Δc^D_1 and Δc^D_2 contributions to the 3IMD ($2\omega_1-\omega_2$ and $2\omega_2-\omega_1$ overlap), for several separations between tones. The intrinsic contributions cannot reproduce the envelope frequency-dependent 3IMD level

The parameter Δc^{D_1} is responsible for second harmonic generation, which in turn mixes with the fundamental frequencies ω_1 and ω_2 , and gives rise to 3IMD. On the other hand, Δc^{D_2} directly generates a certain level of 3IMD distortion. We use the literature value of $\Delta c^{D_2} = -1 \cdot 10^{-10} \text{ N}^{-1}\text{m}^2$ (Lepkowski et al., 2005).

With the above-mentioned values of intrinsic nonlinearity, simulations of 3IMD are performed obtaining values which are below the measured levels, as shown in Fig. 8. This shows that other contributions exist. Figure 9 shows 3IMD measurements at different envelope frequencies, centered at the frequency where the 3IMD is maxima. The measurements reveal a strong dependence with the envelope frequency that cannot be accounted for intrinsic nonlinearities. The dependence of the 3IMD level on the envelope frequency suggests that the 3IMD is dominated by a thermal effect.

3.2.2 Self-heating

The thermal model, as presented in section II.B.3, is implemented by using the literature values of thermal conductivity and specific heat for each layer. The materials stack is composed of more than ten layers. Dissipation on the electrodes and viscous losses are coupled to the thermal domain by means of current sources. By using the model we can determine the temperature distribution along the materials stack, even at different envelope frequencies as shown in Fig. 10. Note that the temperature is almost the same in the piezoelectric layer and the electrodes, which validates the hypothesis in Section II.B.2, of negligible thermal impedance between the electrodes and the piezoelectric layer, to obtain the closed-form expressions.

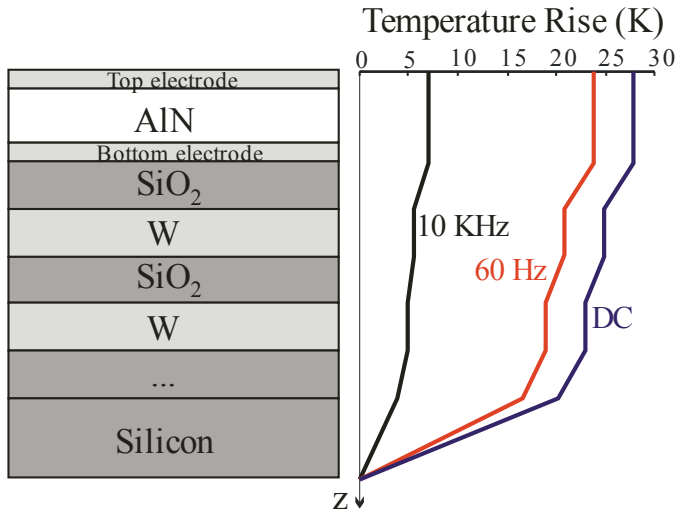


Fig. 10. Simulations of the distribution of the z temperature variation, inside the resonator, calculated with the circuit model. Simulations are done for resonator A1 at $P_{in} = 30 \text{ dBm}$, for different separation between tones

A value of $\Delta c^{D_K}/c^{D_0} = -15 \text{ ppm/K}$ is found to fit the 3IMD best for all resonators. Figure 11 shows the intrinsic and self-heating 3IMD contributions independently as well as the sum of

all contributions, which match the measurements for all the tone separations. The model reproduces very well the measured 3IMD values except the asymmetry between lower and higher 3IMD that appears for envelope frequencies around 6 MHz. This asymmetry is considered to be a consequence of a cancellation between different 3IMD contributions and is currently under investigation.

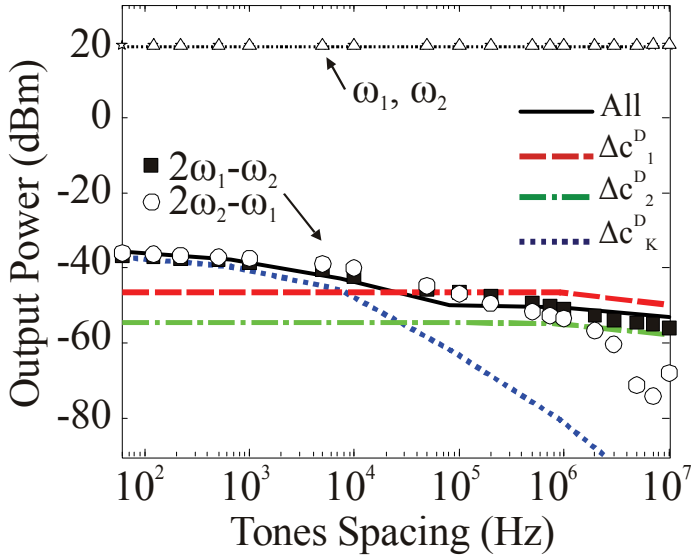
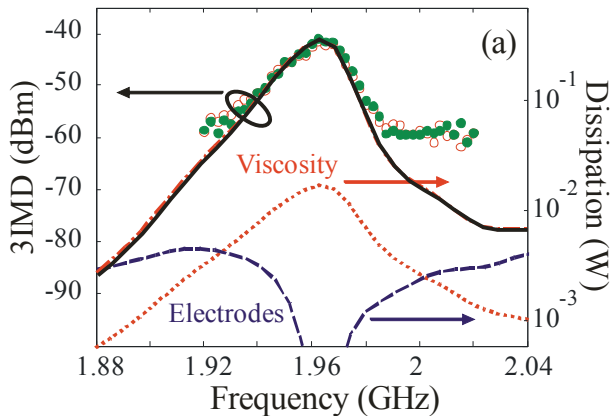


Fig. 11. Measurements (stars, triangles, squares and circles are ω_1 , ω_2 , $2\omega_1-\omega_2$ and $2\omega_2-\omega_1$ respectively) and simulations (thin dotted line is ω_1 and ω_2 , solid line is $2\omega_1-\omega_2$ and $2\omega_2-\omega_1$ overlapped) of the fundamentals and the 3IMD for different tones spacing for A1. The dotted line, the dash-dot line and the dashed line are simulations of the 3IMD contribution due to Δc^D_K , Δc^D_2 and Δc^D_1 respectively. The solid line is the 3IMD simulation with all the nonlinear contributions



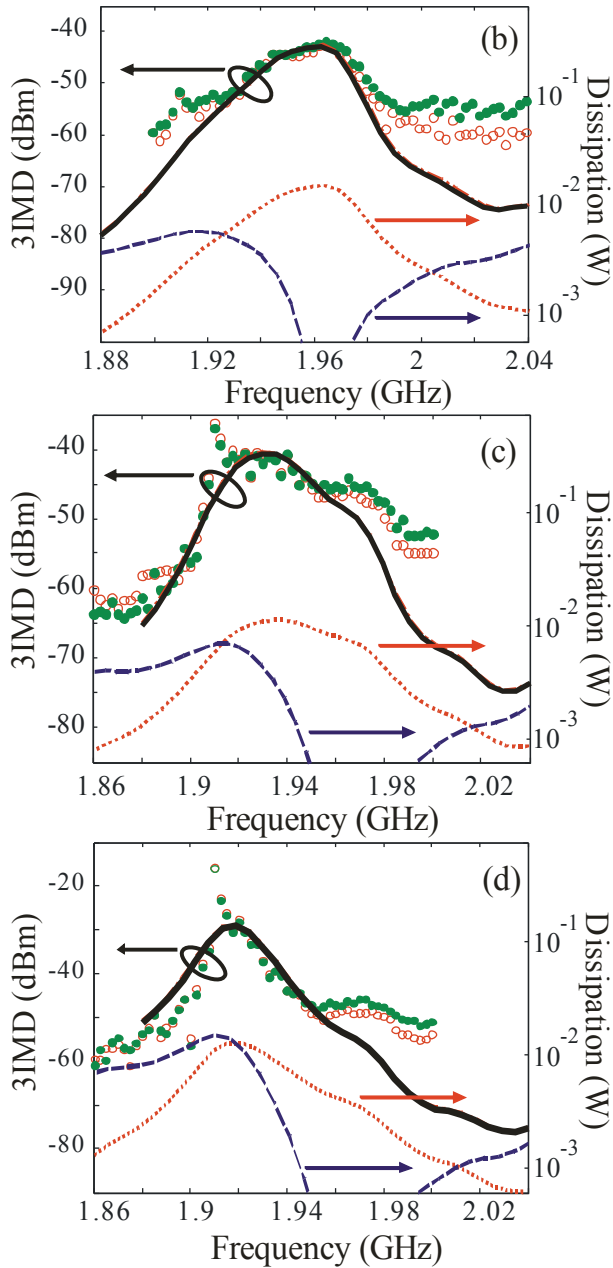


Fig. 12. Measurements (filled circles are $2\omega_1 - \omega_2$, empty circles are $2\omega_2 - \omega_1$) and simulations (solid line is $2\omega_1 - \omega_2$, dash-dot line is $2\omega_2 - \omega_1$) of the 3IMD for resonators A1, A2, A3 and A4 in Fig.12.a, Fig.12.b, Fig.12.c and Fig.12.d respectively. The figures also show the dissipation in the electrodes (dashed line) and in the piezoelectric layer due to viscous losses (dotted line)

Figure 12 shows measurements and simulations of the 3IMD about the frequency range of interest, for each resonator, by use of the circuit model. In this experiment, the two tones are swept around the resonating frequencies keeping the separation between tones constant at 100 Hz. The results show good agreement between simulations and measurements above the nonlinear system baseline level, which is around -60 dBm.

The dashed and dotted lines in Fig. 12 show the simulated dissipated power due to electrodes losses and viscosity respectively, which have different frequency dependences according to the maximum electric current and mechanical stress, respectively. 3IMD measurements for resonators A3 and A4 in Fig. 12 show a peak at the antiresonant frequency that is underestimated by the simulations. The frequency dependence in that range points to a possible electric-field contribution to the 3IMD. This contribution is below the system nonlinear baseline level for resonators A1 and A2, and the area scaling has not been successfully reproduced by use of an electric-field dependent permittivity or stiffened elasticity in the acoustic transmission line, so further research is needed.

4. Conclusion

The role of self-heating and material nonlinearities in the generation of 3IMD in bulk acoustic wave devices has been evaluated through measurements, models and equations. Self-heating is found to have a very significant contribution to 3IMD and thus thermal considerations are critical in the device design. The presented circuit model implementation offers the possibility to predict 3IMD in BAW resonators, given their materials stack and geometry. With such information one can use the resonator model to accurately predict 3IMD in filters. Further research will be performed to investigate the relation between the electric-field contribution to 3IMD and the cancellation shown in the measurements. The development of a 3D equivalent thermal model, to take into account complex heat dissipation through the substrate, will also be investigated.

5. Appendix I – 3IMD equations

At each elemental section, and following a similar process than that described in (Collado et al., 2009), the nonlinear capacitance acts as an infinitesimal nonlinear current generator at $2\omega_1 - \omega_2$ (and $2\omega_2 - \omega_1$), when ω_1 and ω_2 are at resonance:

$$\frac{\partial I_{nl,\omega_2}(z)}{\partial z} = \frac{1}{2} j\omega_2 \Delta C_K K_{\Delta\omega}^* V_{\omega_1} \cos\left(\frac{\pi z}{l}\right) \quad (18)$$

where $K_{\Delta\omega} = Z_{th}(\Delta\omega) P_d(\Delta\omega)$.

Therefore the broadband energy balance all over the acoustic transmission line leads to

$$V_{\omega_2} = -j \frac{1}{2} Q_L \frac{\Delta C_K}{C_{d,0}} P_{d,\Delta\omega} Z_{th,\Delta\omega}^* V_{\omega_1} \left(\frac{1}{j \frac{C_{eq} Q_L}{2W_{0,v}} - 1} \right) \quad (19)$$

6. Appendix II - Model transformation

Losses are introduced as a complex elasticity by means of the viscous damping coefficient η :

$$c \rightarrow c + \eta \frac{\partial}{\partial t} \quad (20)$$

The inverse damping coefficient can also be understood as the conductance per unit length $G_d = \eta^{-1}$. With that, the acoustic telegrapher equations, making use of the analogy between the acoustic and electric domains, can be written as:

$$\frac{\partial V}{\partial z} = -L_d j\omega I \quad (21)$$

and

$$\frac{\partial I}{\partial z} = -\frac{1}{Ac^D + j\omega A\eta} j\omega V. \quad (22)$$

The shunt admittance of the acoustic transmission line implementation, given by (22) and in which $A c^D = C_d^{-1}$, is a shunt capacitance in series with a resistance. To transform this to be a capacitance in parallel with the loss term, we introduce eq. 8 in eq. 22 and expand the shunt admittance in as a Taylor series. The result is a conductance value in parallel with a nonlinear capacitance of the form:

$$C_d(v, K) = C_{d,0} + \Delta C_1 v + \Delta C_2 v^2 + \Delta C_K K \quad (23)$$

whose terms are related with the material linear and nonlinear properties as follows:

$$G = \omega^2 C_{d,0}^2 A \eta \quad (24)$$

$$\Delta C_1 = \frac{c_1^D}{(Ac_0^D)^2} \quad (25)$$

$$\Delta C_2 = -\frac{c_2^D}{A^3 (c_0^D)^2} \quad (26)$$

$$\Delta C_K = -\frac{c_K^D}{A(c_0^D)^2} \quad (27)$$

7. Appendix III - Broadband loaded quality factor

The loaded quality factor can be defined as (Russer, 2006)

$$Q_L = \frac{Q_0}{1 + \beta} \quad (28)$$

where β relates the dissipated power in the acoustic resonator P_{res} , that is the acoustic transmission line, and the externally dissipated power P_{ext} as follows:

$$\beta = \frac{P_{ext}}{P_{res}}. \quad (29)$$

By circuit analysis of the KLM circuit model, it can be found that β is

$$\beta = \frac{\operatorname{Re} \left(\frac{1}{\left(50 + jX_m + \frac{1}{j\omega C_0} \right)^*} \right)}{\operatorname{Re} \left(\frac{1}{\left(Z_{in} - jX_m - \frac{1}{j\omega C_0} \right)^*} \right)} \quad (30)$$

where Z_{in} is the input impedance of the device and X_m is the series reactive term of the KLM model (Krimholtz et al., 1970). Q_0 in (28) represents the unloaded quality factor, that is obtained from S-parameters using (Feld et al., 2008)

$$Q_0 = \omega\tau \frac{|S_{11}|}{1 - |S_{11}|^2} \quad (31)$$

8. References

- Auld B. A., *Acoustic Fields and Waves in Solids* (Krieger, Malabar, Florida), Vol. I, 1990
- Camarchia V., Cappelluti F., Pirola M., Guerrieri S. D., Ghione G. 2007. Self-Consistent Electrothermal Modeling of Class A, AB, and B Power GaN HEMTs Under Modulated RF Excitation. *IEEE Transactions on Microwave Theory and Techniques*, vol. 55, no. 9, Sept. 2007, pp. 1824-1831.
- Cho Y., Wakita J. 1993. Nonlinear equivalent circuits of acoustic devices. *Ultrasonics Symposium, 1993. Proceedings, IEEE 1993*, pp. 867-872 vol. 2, 31 Oct-3 Nov 1993
- Constantinescu F., Nitescu M., Gheorghe A. G. 2008. New Nonlinear Circuit Models for Power BAW Resonators. *ICCSC 2008. 4th IEEE International Conference on Circuits and Systems for Communications*, pp. 599-603, 26-28 May 2008
- Collado C., Rocas E., Padilla A., Mateu J., O'Callaghan J. M., Orloff N. D., Booth J. C., Iborra E., Aigner R. 2010. First-order nonlinearities of bulk acoustic wave resonators. *IEEE Transactions on Microwave Theory and Techniques*, submitted.
- Collado C., Rocas E., Mateu J., Padilla A., O'Callaghan J. M. 2009. Nonlinear Distributed Model for Bulk Acoustic Wave Resonators. *IEEE Transactions on Microwave Theory and Techniques*, vol. 57, no. 12, Dec. 2009, pp. 3019-3029
- Collado C., Mateu J. and O'Callaghan J. M. 2005. Analysis and Simulation of the Effects of Distributed Nonlinearities in Microwave Superconducting Devices. *IEEE Trans. Appl. Supercond.* vol. 15, No. 1, March 2005, pp. 26-39.
- Feld D. A. 2009. One-parameter nonlinear mason model for predicting 2nd & 3rd order nonlinearities in BAW devices. *2009 IEEE International Ultrasonics Symposium (IUS)*, pp. 1082-1087, 20-23 Sept. 2009
- Feld D. A., Parker R., Ruby R., Bradley P., Shim D. 2008. After 60 years: A new formula for computing quality factor is warranted. *2008 IEEE International Ultrasonics Symposium*, pp. 431-436, 2-5 Nov. 2008

- Ivira B., Benech P., Fillit R., Ndagijimana F., Ancey P., Parat G. 2008. Modeling for temperature compensation and temperature characterizations of BAW resonators at GHz frequencies. *IEEE Transactions on Ultrasonics, Ferroelectrics and Frequency Control*, vol. 55, no. 2, February 2008, pp. 421-430.
- Krimholtz R., Leedom D.A., Matthaei G.L. 1970. New equivalent circuits for elementary piezoelectric transducers. *Electronics Letters*, vol. 6, no. 13, pp. 398-399, June 1970
- Lakin K. M., McCarron K. T., McDonald J. F. 2000. Temperature compensated bulk acoustic thin film resonators. *2000 IEEE International Ultrasonics Symposium*, pp. 855-858 vol. 1, Oct 2000
- Larson III J. D., Oshrnysky Y. 2002. Measurement of effective kt_2 , q , R_p , R_s vs. Temperature for Mo/AlN FBAR resonators. *2002 IEEE International Ultrasonics Symposium*, pp. 939- 943 vol. 1, 8-11 Oct. 2002
- Lepkowski S. P., Jurczak G. 2005. Nonlinear elasticity in III-N compounds: Ab initio calculations. *Physical Review B*, vol. 72, 245201, 2005, pp 1-12.
- Nakamura H., Hashimoto K.-y., Ueda M. 2010. Nonlinear effects in SAW and BAW components. *2010 IEEE International Ultrasonics Symposium (IUS), Short Course*, 11-14 Oct. 2010
- Parker A. E., Rathmell J. G. 2004. Self-heating process in microwave transistors. *Workshop on Applications in Radio Science*, Hobart, TAS, Australia, 18-20 Feb. 2004.
- Petit D., Abele N., Volatier A., Lefevre A., Ancey P., Carpentier J.-F. 2007. Temperature Compensated Bulk Acoustic Wave Resonator and its Predictive 1D Acoustic Tool for RF Filtering. *2007 IEEE International Ultrasonics Symposium*, pp. 1243-1246, 28-31 Oct. 2007
- Rocas E., Collado C., Orloff N. D., Mateu J., Padilla A., O'Callaghan J. M., Booth J. C. 2010. Passive intermodulation due to self-heating in printed transmission lines. *IEEE Transactions on Microwave Theory and Techniques*, accepted for publication.
- Rocas E., Collado C., Booth J. C., Iborra E., Aigner R. 2009. Unified model for Bulk Acoustic Wave resonators' nonlinear effects. *2009 IEEE International Ultrasonics Symposium (IUS)*, pp. 880-884, 20-23 Sept. 2009
- Rocas E., Collado C., Mateu J., Campanella H., O'Callaghan J. M. 2008. Third order Intermodulation Distortion in Film Bulk Acoustic Resonators at Resonance and Antiresonance. *IEEE MTT-S International Microwave Symposium Digest*, pp.1259-1262, June 2008.
- Russer P. 2006. Electromagnetics, microwave circuit, and antenna design for communications engineering (Artech House), 2006
- Thalhammer R., Aigner R. 2005. Energy loss mechanisms in SMR-type BAW devices. *2005 IEEE MTT-S International Microwave Symposium Digest*, pp. 4, 12-17 June 2005
- Ueda M., Iwaki M., Nishihara T., Satoh Y., Hashimoto K.-Y. 2008. A circuit model for nonlinear simulation of radio-frequency filters using bulk acoustic wave resonators. *IEEE Transactions on Ultrasonics, Ferroelectrics and Frequency Control*, vol. 55, no. 4, pp.849-856, April 2008
- Vuolevi J. H. K., Rahkonen T., Manninen J. P. A. 2001. Measurement technique for characterizing memory effects in RF power amplifiers. *IEEE Transactions on Microwave Theory and Techniques*, vol. 49, no. 8, Aug. 2001, pp. 1383-1389.